Astronomy & Astrophysics manuscript no. output
May 8, 2023

Comprehensive photometric – spectroscopic study of KIC 7756853: a double-lined system with hybrid δ Sct – γ Dor pulsations and (potential) Rossby modes

A. Samadi-Ghadim[1] and P. Lampens[2]

[1] Max-Planck-Institut für Sonnensystemforschung, 37077 Göttingen, Germany e-mail: samadi@mps.mpg.de
[2] Koninklijke Sterrenwacht van België, Ringlaan 3, B-1180 Brussel, Belgium

May 8, 2023

ABSTRACT

KIC 7756853 is a bright *Kepler* double-lined spectroscopic binary with an orbital period of 99.316 ± 0.020 d. It consists of two A-type stars with $T_{eff_{A,B}}$ = 9700 and 7600 (±300) K and log $g_{A,B}$ = 4.7 and 4.0 (±0.3), where the temperature difference seems to contradict the mass ratio obtained from the orbital solution (q = 0.91±0.06). We analysed the entire *Kepler* LC light curve (Q0-Q17) and compared it to the *Kepler* SC (Q1) and TESS data (sectors 14-15, 40-41, 54-55). In total, we detected 20 p modes with $f \leq 25$ d^{-1}, three p modes with $f \geq 25$ d^{-1} in the SC light curve, and 13 g modes without any regular period spacing. We identify the very dominant low frequency of 0.8914 d^{-1} as the rotation frequency $f_{\rm rot}$ of the secondary component (with $v \sin i = 51$ km s^{-1}), and propose an orbital inclination of at most 27°. We detected a group of most dominant independent modes $f \leq 3 f_{\rm rot}$ which are suggestive of (potential) r modes . Due to the coupling between the detected p and g modes and the rotation frequency, we suggest that the secondary is a hybrid δ Scuti – γ Dor pulsator. We report a (probably false-positive) detection of very high frequencies (~319 d^{-1}) from the TESS 54-55 (2-min) and (~391 d^{-1}) the *Kepler* SC light curves that might suggest the presence of roAp pulsations. However, due to their barely significant S/N (slightly larger than 4) and the lack of high-resolution spectra for abundance analysis, we can not confirm their roAp-like nature.

Key words. (Stars:) binaries: spectroscopic - Stars: fundamental parameters - Stars: oscillations (including pulsation) - Stars: variables: δ Scuti - Techniques: photometric

1. Introduction

Pulsations of type γ Dor, δ Scuti and roAp may be excited in A/F-type variable stars located at the intersection of the main sequence and the Cepheid instability strip. Such stars have temperatures $T_{\rm eff}$ = 9800 - 6000 K and luminosities L = 43 - 2 $L_\odot$ (Cox 2000). These classical pulsators experience a change in the main regime of energy transport in their stellar envelope (Christensen-Dalsgaard 2000; D'Antona et al. 2002). Hence, due to the structural modification, different driving mechanisms are exciting pulsations in these stars. The first subgroup, the (low- and high-amplitude) δ Scuti stars are early A- to early F-type stars with masses between 1.5 and 2.5 $M_\odot$ and $T_{\rm eff}$ from 6900 to 8900 K (Breger 2000). The κ mechanism in the partial ionization zone of He II causes excitation of the p modes in the frequency range 4-60 d^{-1}with amplitudes up to 1-2 mmag (Aerts et al. 2010). Recent studies (Antoci et al. 2014; Xiong et al. 2016) present turbulent pressure as another driving mechanism responsible for driving p modes of moderate radial orders. While a δ Scuti star evolves, its Fourier spectrum of the light variation reveals a forest of low(er) frequencies of the type that occurs in γ Dor stars (Handler 2013; Balona & Dziembowski 2011). γ Dor pulsations are excited in mid-F- to late-A-type stars with masses in the range 1.4-1.9 $M_\odot$. The pulsation modes are low-degree, high-order non-radial g modes with periods ranging from 7 hr to 3 d (Kaye et al. 1999) (0.3 $\leq f \leq$3 d^{-1}). The driving mechanism is the flux modulation at the base of the convective zone (Guzik et al. 2000; Dupret et al. 2004, 2005; Grigahcéne et al. 2010). Rapidly oscillating Ap stars (roAp) are chemically peculiar A(-B)-type Ap pulsating stars with abundances of rare earth metals like Si and Cr. and very strong global magnetic fields (up to 35 kG) (Kurtz 1978). They are pulsating in low-degree non-radial modes with 5-24 min periods. The excitation mechanism for these types of pulsations is not clear yet, but one possibility is the κ mechanism in the H I ionization zone (e.g. Balmforth et al. 2001; Saio 2005). Some studies suggest that turbulent pressure could drive these pulsations that may appear either as a single mode or as a rotationally-split multiplet (Cunha et al. 2013).

Detecting A- and F-type pulsators is very difficult from the ground due to the low amplitudes. Thanks to the new generation of space missions (exoplanets and asteroseismology) e.g. *Kepler* (Koch et al. 2010) and Transiting Exoplanet Survey Satellite TESS (Ricker et al. 2014, 2015), we can dispose of unprecedented photometric observations with accuracies of the order of μmag. The availability of these observations has lead to the detection of hundreds of new pulsating A- and F-type stars. We used both the Long Cadence LC (~29.4-min) and the Short Cadence SC (~ 1-min) observations from *Kepler* , and the short cadence TESS observations of 2-min cadence to detect and study pulsation modes of type γ Dor, δ Scuti (e.g. Uytterhoeven et al. 2011; Antoci et al. 2019), or roAp (e.g. Holdsworth et al. 2021). The *Kepler* and TESS observations in recent decades revealed A- and F-type stars with hybrid pulsations where either δ Scuti- and γ Dor-type (e.g. Samadi-Ghadim et al. 2022) or δ Scuti- and roAp-type pulsations (e.g. Murphy et al. 2020) show up on their Fourier spectrum. The mode driving mechanism for none of the two hybrid types is well-understood. Like all classical pulsators, in the stars with hybrid δ Scuti- and γ Dor pulsations, we ex-

Table 1. A summary of previous studies concerning hybrid γ Dor – δ Scuti pulsations in binary stars.

ID	Type[a]	e[b]	Period d	$v \sin i_{1,2}$ km s^{-1}	$M_{1,2}$ $M_\odot$	g modes d^{-1}	p modes d^{-1}	Act.[c] Cycle (d)
KIC 4544587[1]	EB	0.29	2.19	86.5	1.98	γ Dor & tidal[d]	δ Sct	-
				75.8	1.60	0.04-4.57	38.2-48.05	
KIC 10080943[2]	EB	0.45	15.34	19.0	2.0	rot.-split[e]	rot.-split	-
				18.7	1.9	0.6-1.45	12-20	
KIC 6048106[3]	EB	0.01	1.56	-	1.55	γ Dor	tid.-split[f]	spot
				-	0.33	1.96-2.85	7.49-15.2	290
							19-22.5	
KIC 4142768[4]	EB	1.0	13.99	8.67[g]	2.05	γ Dor & tidal	δ Sct	-
	SB2			7.35[g]	2.05	0.1-3.0	15-18	
KIC 8975515[5]	SB2	0.41	1603	162	0.83 (q[h])	rot.-split + r modes (?)	rot.-split	-
				32		1.56-6.18	7.2-21.2	
TIC 11491822[6],[i]	EB	0.078	9.94	-	1.94	γ Dor & tid.-split	δ Sct	-
				-	1.51	0.11-3.51	5.09-18.9	
KIC 9850387[7]	EB	0.0	2.74	13.4	1.66	γ Dor & tid.-split	δ Sct	-
				-	1.06	0.11-3.51	10.7-16.6	
KIC 6951642[8]	SB1	0.25	1796	123	-	rot.-split	rot.-split	spot (?)
				-	-	≥ 0.7	10-17	118
KIC 3440495[9]	ph. mod[j]	-	2414	239	1.5	γ Dor	δ Sct	
				279	1.65	≥ 0.637	13-24.3	

References. (1) Hambleton et al. (2013) (2) Schmid et al. (2015); Keen et al. (2015) (3) Samadi-Ghadim et al. (2018b,a), Lee (2016) (4) Guo et al. (2019) (5) Samadi-Ghadim et al. (2020) (6) Southworth (2021) (7) Sekaran et al. (2020); Zhang et al. (2020); Sekaran et al. (2021) (8) Samadi-Ghadim et al. (2022) (9) Ma et al. (2022)

Notes.
[a] Type i.e. binary classification: EB: Eclipsing Binary, SB2: double-lined Spectroscopic Binary. [b] e: eccentricity [c] Act.: any signature of stellar **Act**ivity [d] tidal: **tidal**ly excited modes [e] rot.-split: **rot**ationally-**split** modes [f] tid.-split: **tidal**ly-**split** modes [g] $v \sin i$ from model [h] q = M_2/M_1: the mass ratio [i] RR Lyn [i] the binarity inferred from pulsational phase modulations.

pect the κ mechanism for p modes (Handler 1999; Houdek et al. 1999; Balona et al. 2015) and convective flux blocking (Guzik et al. 2000; Dupret et al. 2004, 2005) for the g modes to be the main mode driving force. Xiong et al. (2016) theoretically differentiated driving mechanisms for simultaneous excitation of p modes and g modes in hot and cold δ Scuti – γ Dor stars. They believe the (radiative) κ mechanism is the main mechanism in the former type, and the coupling of convection and oscillations is the main mechanism in the latter type of stars. Several hybrid pulsating A- and F-type stars are detected in binary systems, from recent observations. This is an expected fact after Duchêne & Kraus (2013) estimate the fraction of intermediate-mass stars in multiple systems to be more than 50%. The presence of the pulsating companions in the binary systems not only provides additional tools to determine stellar parameters, like in eclipsing and double-lined spectroscopic systems, but also enables us to study the influence of the binarity on the stellar pulsations (e.g. tidal effects Guo et al. 2017; Samadi-Ghadim et al. 2018a; Van Reeth et al. 2023), stellar structure and stellar evolution. Similarly, the presence of a third body (Samadi et al. 2010) or the detection of the binary nature of a star (Murphy et al. 2018) are of another importance in studying stellar oscillations in binaries. Recently, (Lampens 2021) summarised the detections of pulsating components in eclipsing binary stars. Several pulsating binaries are also detected in spectroscopic binaries. Following Moe & Di Stefano (2017), 30-45% of field intermediate-mass stars reside in a spectroscopic binary system. According to a recent spectroscopic study by Lampens et al. (2018) out of 50 *Kepler* hybrid stars the multiplicity fraction of 27% is detected. In Table 1, we list all of the recent detection of A-F-type stars in binary systems with a Hybrid (γ Dor, δ Scuti) pulsating companion(s). In this paper, we investigated a particular case of double-lined spectroscopic star of *Kepler* with significant both low- and high frequencies and a candidate member for the hybrid δ Scuti-γ Dor class.

KIC 7756853 is a *Kepler* main-sequence star of the hybrid (δ Scuti- γ Dor) class (Uytterhoeven et al. 2011) with a spectral type of A3V, $T_{\rm eff}$ = 8060±290 K and $\log g$ = 3.95±0.3, whose Ca II K line was found to be unusually shallow (Niemczura et al. 2015). Niemczura et al. (2015) didn't report any trace of chemical abnormality though they couldn't finish the chemical study due to the double-lined spectrum of the binary. Balona & Dziembowski (2011) previously assumed that the frequency of the highest amplitude in the frequency range $0.1 \leq f \leq 5.0$ d^{-1} is the rotation frequency. From a frequency analysis of the *Kepler* light curves, Balona (2013) suggested a rotation frequency equal to 0.891 d^{-1}(P = 1.12 days) with an amplitude of 0.034 mmag. Later, Barceló Forteza et al. (2020) analyzed more than two thousand of these classical pulsators using the high-cadence TESS light curves. The authors determined the frequency of

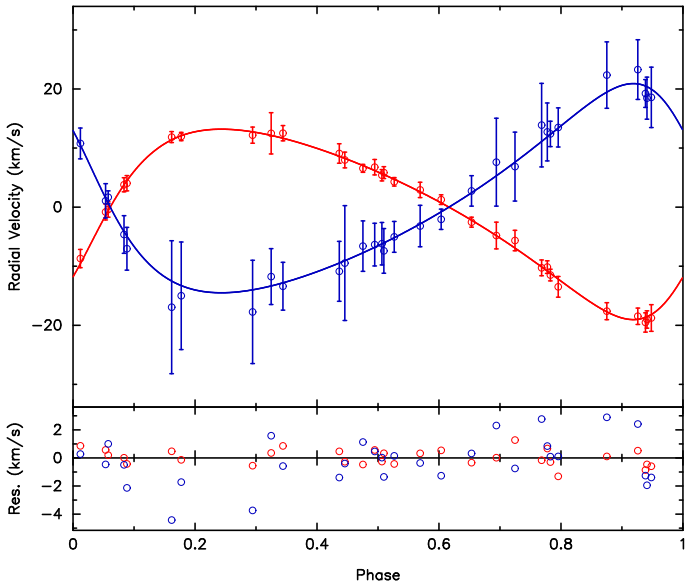

Fig. 1. Radial velocities and best-fit orbital solution for the double-lined spectroscopic system KIC 7756853. Residuals are shown versus the orbital phase in the bottom panel.

maximum power for each star and proposed to use this frequency as a proper seismic index since it is directly related to the intrinsic stellar parameters (temperature, mass, and radius). For KIC 7756853, they measured a large separation of 220 ± 20 μHz (equivalent to 19.0 d^{-1}) and proposed an effective temperature T_{eff} = 7800±200 K, $\log g$ = 3.85, a minimum rotation rate of 70% of the break-up frequency and an upper limit of 43° for the inclination. However, their measured T_{eff} was 8300±300 K. We selected this object for an extensive asteroseismic study based on the quasi-continuous space-based light curves on the one hand and the spectroscopic analysis by Lampens et al. (2018) on the other hand, because of the win-win scenario of a hybrid pulsator in a twin-like binary.

In Sect. 2, we report the results of our spectroscopic study. We describe the available photometric observations Sect. 3. The methodology of Fourier analysis is explained in Sect. 4. We report the results of our frequency analysis in the search for δ Scuti pulsations in Sect. 5 and γ Dor pulsations in Sect. 6. In the end, we discuss our results in Sect. 7.

2. Spectroscopic results and orbital parameters

Following up on the work by Uytterhoeven et al. (2011), Lampens et al. (2018) classified KIC 7756853 as a double-lined spectroscopic binary (SB2) based on a homogeneous set of multi-epoch spectra. The composite spectrum was matched with a model consisting of an A1-type primary and an A5 to F0-type secondary, with a difference in $v \sin i$ of only 20 km s^{-1} between both. Lampens et al. (2018) derived the following atmospheric parameters for the components: $T_{eff,1}$ = 9980 ± 120 K and $T_{eff,2}$ = 7300 ± 140 K, adopting the light factor l_1 = 0.66 ± 0.04 and log g = 4. The previous value of T_{eff} likely corresponds to some mean value (without consideration of the SB2 character). The spectra were acquired with the spectrograph HERMES installed at the Mercator telescope (REF), La Palma, Spain, and the Coudé échelle spectrograph (TCES) (REF) of the Thüringer Landessternwarte, Tautenburg, Germany. Thirty-one high-resolution spectra of KIC 7756853 were gathered over a period of over 11 years (see Table A1 see Annex for general properties of the spectra). The component radial velocities were extracted as explained by Lampens et al. (2018). Table 2 lists the orbital parameters with their respective standard deviations corresponding to the best-fitting solution shown in Fig. 1. The long-term monitoring and the homogeneous phase coverage allowed us to derive the orbital period accurately. As can be seen from Fig. 1 and Table 2, the components have similar radial velocity amplitudes with respect to the center of mass, which indicates that they must have similar masses. Component A (in red in Fig. 1), the most massive component, is also the apparently slower rotating star ($v \sin i$= 31 ± 2 km s^{-1}), while component B

Table 2. Values and standard deviations of the constrained parameters of the orbital solution for KIC 7756853.

Orbital solution A-B		
Parameter	Value	Stand. dev.[a]
P_{orb} (d)	99.316	$^{+0.020}/_{-0.019}$
T_0 (HJD)[b]	2458498.5	$^{+0.8}/_{-0.8}$
e	0.33	$^{+0.02}/_{-0.02}$
ω (°)	236.6	$^{+3.3}/_{-3.4}$
V_0 (km s^{-1})	-21.6	$^{+0.2}/_{-0.2}$
K_A (km s^{-1})	16.11	$^{+0.37}/_{-0.37}$
K_B (km s^{-1})	17.7	$^{+1.1}/_{-1.1}$
$a_A \sin i$ (AU)	0.140	0.003
$a_B \sin i$ (AU)	0.153	0.009
$M_A \sin^3 i$ ($M_\odot$)	0.175	0.022
$M_B \sin^3 i$ ($M_\odot$)	0.160	0.012
rms_A (km s^{-1})	0.56	(with v sin i = 31 km s^{-1})
rms_B (km s^{-1})	1.69	(with v sin i = 51 km s^{-1})

Notes. [a] Standard deviation [b] Time of periastron passage in Heliocentric Julian Date

Table 3. Information from the literature, surveys, and large databases.

Catalogue	Number
HD	184449
KIC	7756853
TIC	275493853
Gaia DR3	2125886971888144000
Parameter (Unit)	**Value**
(RA, Dec) (deg)	(293.163, 43.436)[3]
ϖ (mas)	2.502±0.05[3]
distance (pc)	396.891[4]
Kp (mag)	8.958[1]
Tmag	8.79477[2]
Gaia mag	8.895614[3]
Contamination	0.015[1]
	0.028[2]
E(B-V) (mag)	0.026[5]
G_{Bp} - G_{Rp} (mag)	0.203[3]

References. (1) Brown et al. (2011) (2) Stassun et al. (2019) (3)Halbwachs et al. (2022) (4)Bailer-Jones et al. (2021) (5) Capitanio et al. (2017)

Table 4. Available photometry observations from TESS mission for KIC 7756853.

author	sector	date	Cadence min	obs. days	pause days	pause reason
TASOC[(a)], QLP[(b)]	14	2019-07-18 to 2019-08-14	2,30	25.91	0.95	perigee passage
TASOC, QLP, TESS-SPOC[(c)]	15	2019-08-15 to 2019-09-10	2,30	24.97	1.08	perigee passage
TESS-SPOC, QLP, SPOC[(d)]	40	2021-06-25 to 2021-07-23	2,10	27.28	0.93	data downloading
TESS-SPOC, QLP, SPOC	41	2021-07-24 to 2021-08-20	2,10	25.48	1.11	data downloading
SPOC	54	2022-07-09 to 2022-08-04	2	25.05	1.19	data downloading
SPOC	55	2022-08-05 to 2022-09-01	2	26.26	0.91	data downloading

Notes. obs.: Science data observation period
[(a)] TESS data For Asteroseismology Light curves (Lund et al. 2015, 2017).
[(b)] TESS light curves from the MIT Quick-Look pipeline (Kunimoto et al. 2021; Huang et al. 2020b,a)
[(c)] TESS light curves from Full Frame Images (Caldwell et al. 2020)
[(d)] The TESS data processing pipeline developed by the Science Processing Operations Centre (Jenkins et al. 2016).

($v \sin i$= 51 ± 2 km s^{-1}, in blue in Fig. 1) is slightly less massive than its companion. The rms of the radial velocity (RV) residuals is about three times larger for component B than for component A (cf. Table 2), which may indicate that it is subjected to pulsations. However, all the spectra show blended composite profiles which makes it difficult to extract the atmospheric properties of the components in a precise way. Therefore, we adopted the fractional luminosities l_1 = 0.6 (comp A) and l_2 = 0.4 (comp B) and used the technique of spectral separation. The best set of atmospheric parameters estimated for component A is $T_{\rm eff}$ = 9700 ± 300 K, log g = 4.7 ± 0.3 (cgs), while that for component B is $T_{\rm eff}$ = 7600 ± 300 K, log g = 4.0 ± 0.3 (cgs). These values are also in very good agreement with our first results (Lampens et al. 2018).

3. Photometric observations

KIC 7756853 is a bright *Kepler* star of magnitude Kp = 8.958 mag (Brown et al. 2011). The relevant astrometric and color information available from different surveys is presented in Table 3 Info to appear in the Intro. From the *Kepler* mission, observations (Q0-Q17 with a four-year long time base, T = 1437.420 days) in LC mode and an additional series of observations in SC mode from quarter Q1 (2009-05-13 to 2009-06-15 with T = 33.491 days) are available. During its mission, TESS observed KIC 7756853 on three different occasions in pairs of consecutive sectors with 2-, 10-, and 30-min cadences. Table 4 lists the sectors, dates, cadences, time spans, and intervals of the observational gaps for all the TESS observations for this particular star.
In view of a pulsation study, we normalised the PDCSAP flux from all the LC quarters to the median value. We used the limit of twice the standard deviation, $2\sigma_{\rm flux}$, to exclude outliers and converted the fluxes to the magnitude scale. We applied the LightKurve (Lightkurve Collaboration et al. 2018) python package stepwise. We performed the same steps to 'detrend' the *Kepler* SC light curve, except for a $3\sigma_{\rm flux}$ lower limit for the exclusion of outliers. We present a closer view of the detrended *Kepler* light curves in panels (a) and (b) of Fig. 2. Since the systematic errors were not completely removed in the PDCSAP flux of the quarters Q6-Q7 (e.g. Jenkins (2017)), we tried smoothing the light curves by flattening (with a Savitzky-Golay filter) and customisation of the Target Pixel Files (TPF). These steps did not lead to the introduction of any extra significant frequency (sect. 4), but removed the lowest frequencies ($f \leq 0.1$ d^{-1}) from LC Fourier spectra.
We used a similar procedure for the TESS data. We present the TESS-SPOC and TASOC light curves of sectors 14-15 (30 min and 2-min) in panels (c) and (d) of Fig. 2. The SPOC light curves of sectors 40-41 and 54-55 are displayed in panels (e) and (f). we also computed the corrected SAP fluxes Lund et al. (2021) assuming eight co-trending basis vectors (CBV), for 2-min observations, due to the larger amplitude of light variation (4 mmag) in comparison to 30-min observations (0.8 mmag). We present the light curves from *Kepler* and TESS phased against the orbital period with respect to the epoch of periastron passage, T0 = HJD 2458498.5 (Table 2), in Fig. 3. Accordingly, we observe that there exists neither TESS nor *Kepler* data (in SC mode) of KIC 7756853 any time close to periastron passage.

4. Fourier analysis

We employed the Lomb-Scargle periodogram (Lomb 1976; Scargle 1982) for the frequency analysis. For each data set of Table 5, we calculated the Fourier spectrum up to the Nyquist value (cf. $f_{\rm Nyq}$ in Table 5). The signal-to-noise ratio, S/N, is the mean over a window of width 2d^{-1}. We consider any frequency as a 'significant' candidate for a pulsation mode if S/N≥4 (Breger et al. 1993). These significant frequencies are derived by iteratively fitting a sinusoid with the frequency of the highest amplitude and removing it from the original spectrum. Two significant frequencies, f_i and f_j, are assumed to be well-resolved if $|f_i - f_j| \leq 1.5/{\rm T}$, with T the time span of the observations (e.g. Aerts et al. 2010). For each spectrum, $f_{\rm res}$ is reported in Table 5. Figures 4 and 5 illustrate the significant frequencies extracted from the Fourier spectrum of the *Kepler* and TESS light curves. Fig. 5 excludes the frequency ranges $f \geq 30$ d^{-1}for SC and $f \geq 24.47$ d^{-1}for the TESS (2-min) light curves in panels (b, d, f, and h) due to the absence of any significant frequency. We summarise the number of significant frequencies extracted from each data set in Table 5 along with the characteristics of the most dominant frequency in each spectrum. Next, we selected the parent frequencies to have the largest amplitudes and S/N in different regions in order to try and recognise combination and harmonic frequencies of such modes. We performed a search for unique linear combinations or harmonics of the parent frequencies considering the resolution frequency, i. e. $|f_{\rm cal} - f_{\rm detected}| \leq f_{\rm res}$, $f_{\rm cal}$ the calculated harmonic frequency. We illustrate the detected combinations with dotted blue lines in Fig. 4. We followed the same procedure to recognise the combinations or harmonics of the orbital frequency $f_{\rm orb}$ = 0.010

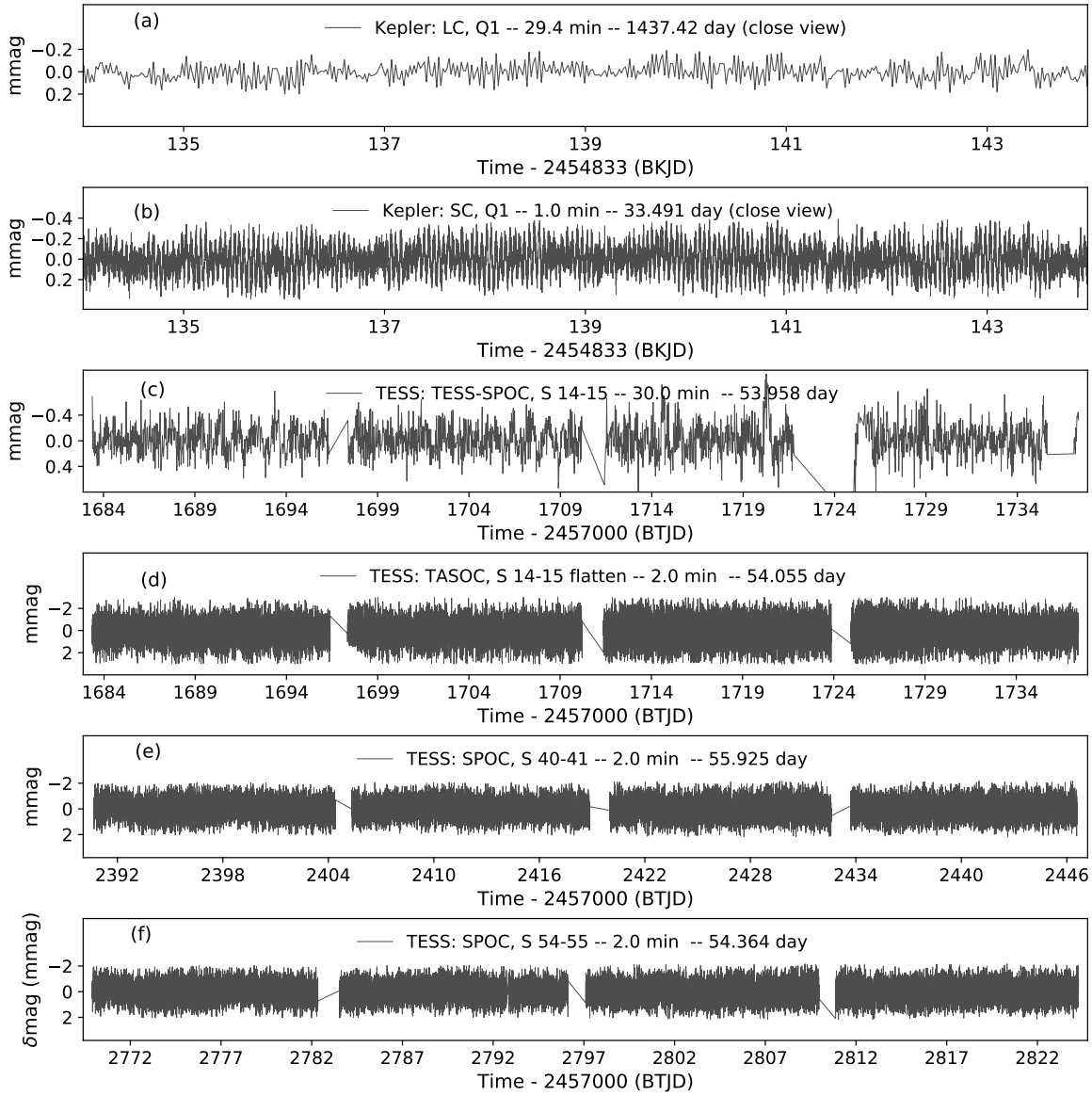

Fig. 2. A close view to KIC 7756853 light curves from *Kepler* LC, SC-Q1 observations and TESS sectors 14-15, 40-41, and 54-55 observations.

± 0.00002 d^{-1}. From the *Kepler* LC data set, we detected several frequencies that could mathematically agree with very high orbital harmonics. We marked these potential harmonics of $f_{\rm orb}$ with a (?) in Sect. 5.1 (Table 7) and 6.1 (Table 11). The list of significant frequencies and the results of the searches for combinations and harmonics are reported separately for the high- and low-frequency regions, respectively in Sect. 5.1 (Table 7) and 6.1 (Tables 11 and 12). These frequencies are sorted according to decreasing amplitude. Concerning the *Kepler* SC and TESS data sets, the results are presented in Tables 9, 14, 10 and 15, respectively. In these tables, we report the linear combinations and harmonics under the column 'comb', where we indicate the parent frequencies by the letter 'P'. The associated uncertainties in frequency and amplitude are mentioned in Table 6.

5. Detection of δ Scuti-type pulsations

5.1. The Kepler LC light curve

We present a portion of the high-frequency region of the *Kepler* LC spectrum ($f \geq 17.5$ d^{-1}) in Fig. 6, where we indicate the parent frequencies located in four different regions (Table 7). We discuss the parent frequencies similar to Fig. 6. The most dominant frequency in the *Kepler* LC spectrum, $f_1 = 21.1416$ d^{-1}(panel (b) in Fig. 6), doesn't appear in any linear combination. The second most dominant frequency in the *Kepler* LC spectrum, $f_2 = 20.7177$ d^{-1}, shows up in three different combination types:

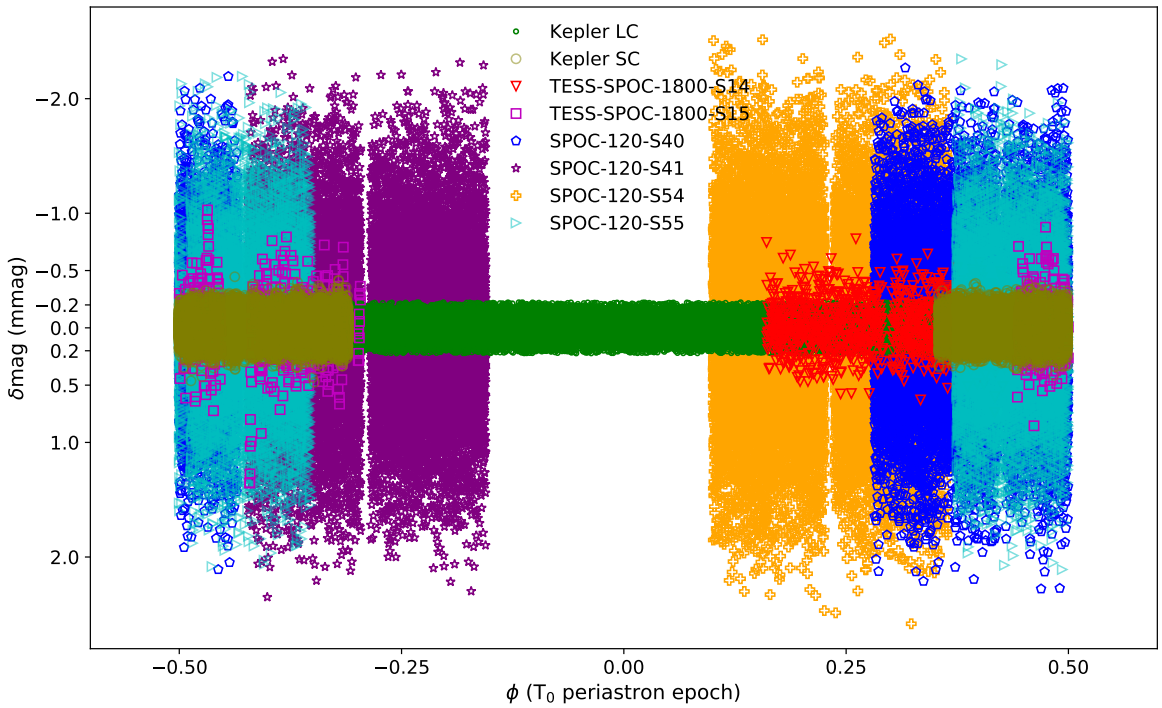

Fig. 3. Phase plot for the *Kepler* and TESS light curves using T0 equal to HJD 2458498.5 (cf. Sect. 2).

Table 5. Characteristics of the Fourier spectra obtained from different data sets.

Q/S	T d	Δt min	T0 BKJD/BTJD	f_{res} d^{-1}	f_{Nyq} d^{-1}	N_{freq}	f_1 d^{-1}	A_1 mmag	S/N_1
Kepler									
0-17	1437.420	29.4	120.5389	0.000696	24.47	179	21.1416±2×10^{-6}	0.078±4×10^{-7}	195
1	33.491	1	131.5023	0.0299	734.1	26	21.1415±0.0001	0.107±0.001	29
TESS									
14-15$^{(a)}$	53.958	30	1683.3883	0.0185	24.0	7	21.1402±0.0011	0.07±0.008	8
14-15$^{(b)}$	54.055	2	1683.3883	0.0185	360.0	6	0.0937±0.0004	0.17±0.006	9
40-41$^{(c)}$	55.925	2	2390.6557	0.0179	360.0	6	21.1416±0.0005	0.1±0.005	13
40-41$^{(d)}$	55.925	2	2390.6557	0.0179	360.0	11	0.0897±0.0001	0.394±0.006	13
54-55$^{(c)}$	54.363	2	2769.9016	0.0184	360.0	6	0.0977±0.0006	0.085±0.005	8
54-55$^{(d)}$	54.363	2	2769.9016	0.0184	360.0	8	0.0937±0.0004	0.168±0.006	9

Notes. Q/S: *Kepler* Quarter or TESS Sectors. T: Time span. Δt: Time sampling. BKJD: Barycentric *Kepler* Julian Date. BTJD: Barycentric TESS Julian Date. N_{freq}: number of derived significant frequencies.
$^{(a)}$ TESS-SPOC , $^{(b)}$ TASOC , $^{(c)}$ SPOC , $^{(d)}$ CBV corrected.

a. Coupled with the third and fourth harmonics of f_{orb}, f_2 (panel (b) in Fig. 6) leads to a couple of frequencies centred at 20.6 d^{-1}(see [e. g.] f_{172} and f_{153} in Table 7).
b. Coupled with a g mode , f_2 produces a p mode ($f_{53} = f_9 + f_2$) located around 23.15 d^{-1}(see panel (d) of fig. 6). We indicate this type of combination with Mode Coupling 'MC' in Tables 7, 9.
c. Coupled with another parent frequency, f_2 may generate a g mode , that is to say, $f_{142} = 2f_{12} - 2f_2$. We indicate this type of combination with (*) in Tables 11 and 14. One may consider the described coupling as another presentation of above mentioned type (b). The fact that in this kind of coupling (e.g. f_{12}) the contributing g mode is a more significant mode (with a higher amplitude) than the identified p mode (e.g. f_{142}), we suggest the here mentioned coupling to be different than type (b).

We detected several frequencies that are (potentially) agreeing very well with very large harmonics of f_{orb}. We added a note for these frequencies, a question mark (?), in Table 7, and we highlighted them with dotted green lines (labelled as nf_{orb}) in Fig. 6. Overall, we identified 22 independent p modes (with S/N ≥ 5), seven of which were assumed to be parent p modes .
According to the spectroscopic analysis, KIC 7756853 is an ec-

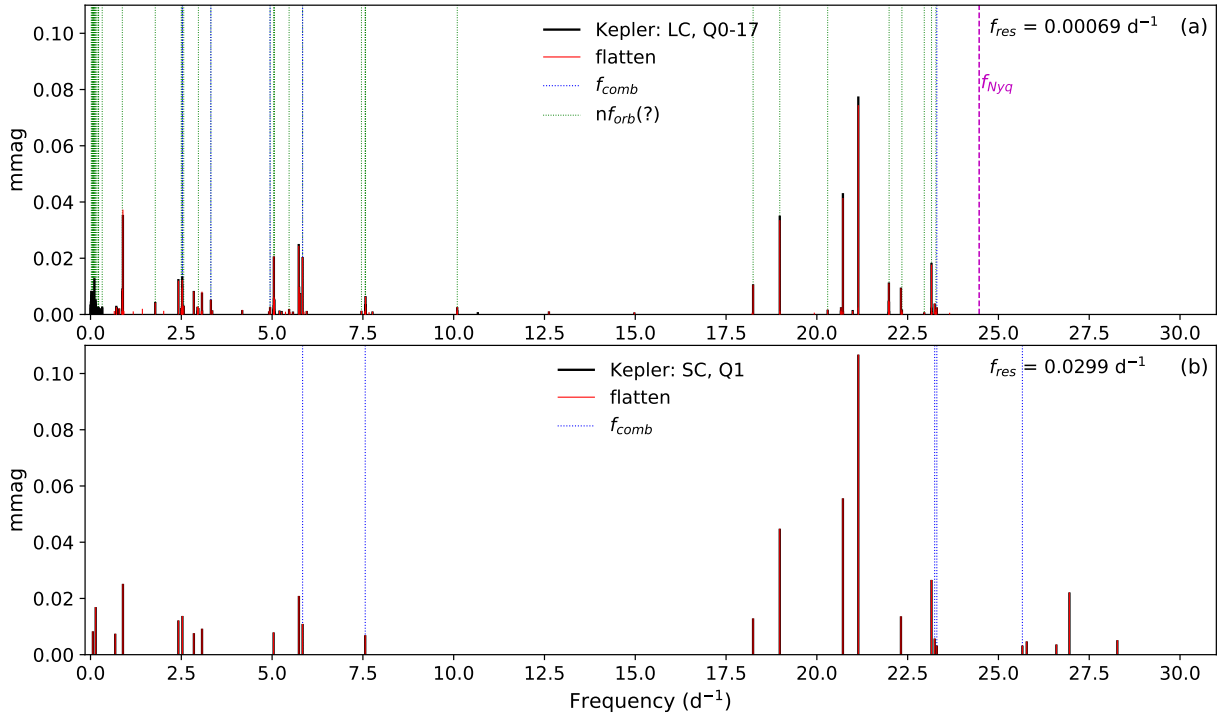

Fig. 4. Detected significant frequencies from KIC 7756853 *Kepler* LC and SC datasets.

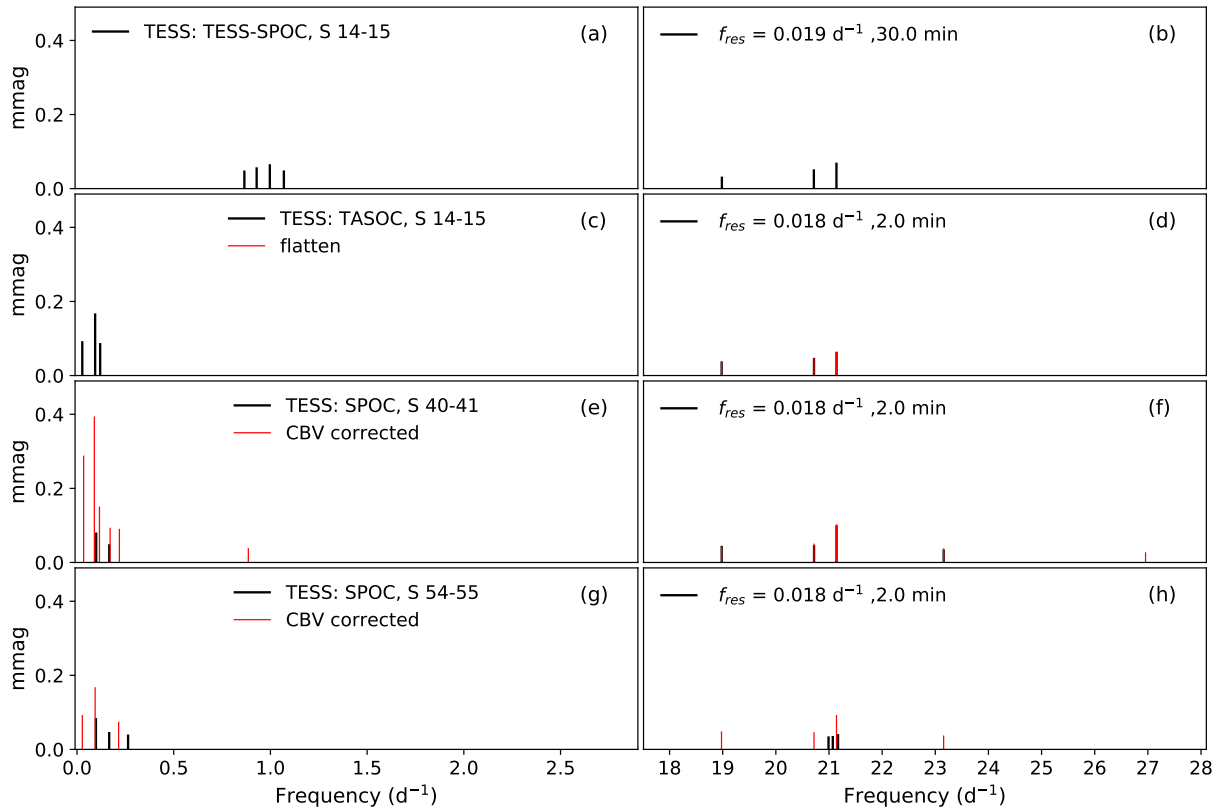

Fig. 5. Detected significant frequencies from KIC 7756853 TESS (30-min and 2-min) datasets.

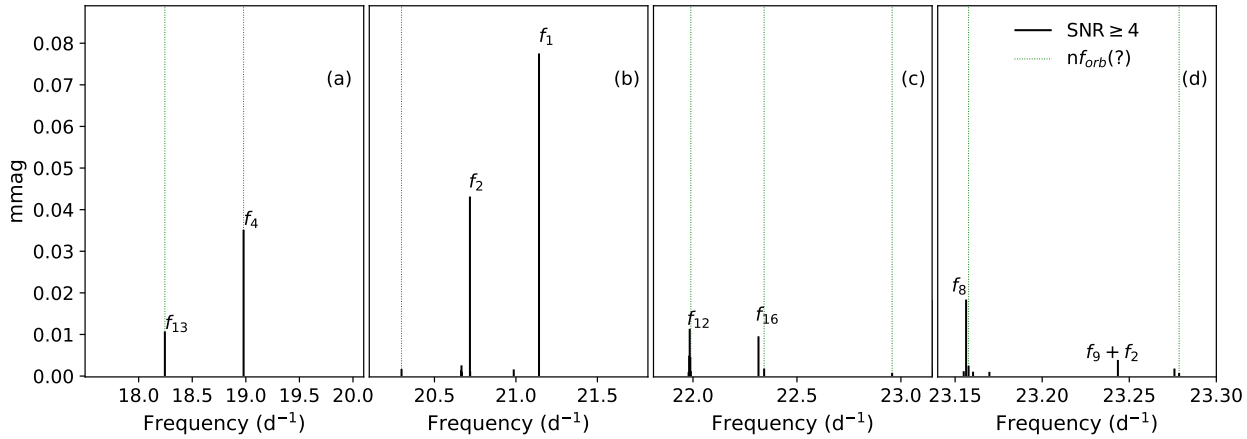

Fig. 6. Well-resolved significant frequencies in the high-frequency region of the *Kepler* LC spectrum.

Table 6. Frequency and amplitude uncertainties of the significant frequencies detected in different observations.

Obs.	min(ϵ_f) d^{-1}	max(ϵ_f) d^{-1}	min(ϵ_A) mmag	max(ϵ_A) mmag
Kepler				
LC	2×10^{-6}	0.0001	0.0002	0.0004
SC	0.0001	0.003	0.0005	0.0007
TESS				
s14-15 (2-min)	0.0004	0.0016	0.006	0.0068
s14-15 (30-min)	0.0011	0.0022	0.0069	0.0075
s40-41	0.0001	0.0018	0.0051	0.0061
s54-55	0.0004	0.0021	0.006	0.0442

centric binary system with an eccentricity e = 0.33 (Table 2), and we have access to 14 orbital cycles from the *Kepler* LC data set. We investigated whether any p mode could be tidally influenced by observing its evolution through the orbital cycles. Thus, we binned the LC light curve into bins with a mean time span of T_{mean} = 27.47(80) ± 3.07(22) days (equivalent to approximately one quarter of the orbital period with $f_{res,mean}$ = 0.036 ± 0.003 d^{-1}). We applied Fourier analysis in the same way as in Sect. 4. For detailed information on the start and end dates (expressed in BKJD), orbital phases, time spans, and f_{res} of each bin, see Table A2. In Fig. A1, we present our results for the six (most) dominant p modes f_1, f_2, f_4, f_8, f_{12} and f_{16}. The top rows of Fig. A1 display the evolution of the amplitude across the orbital cycle, and the bottom rows show the corresponding phase evolution. The reported σ's are the standard deviations of the amplitudes or phases. We didn't distinguish any amplitude or phase evolution for the frequencies through the orbital phase.
in the search for frequency-splitting, we recognised two regular splitting patterns among the p modes : 1) a small frequency spacing $\Delta f \sim 0.0027$ d^{-1}(corresponding to $\sim$ 1 yr^{-1} or 1/370 d (we doubt that such spacing has a physical cause), 2) a common frequency spacing $\Delta f \sim 0.84$ d^{-1}detected in several doublets where the dominant p modes f_1, f_8, f_{12} and f_{16} appear. Table 8 reports on the detected frequency splittings.

Table 7. Well-resolved significant frequencies in the high-frequency region of the *Kepler* LC spectrum.

f_i	f (d^{-1})	A (mmag)	S/N	comb.
f_4	18.9791	0.0352	139	P ?
f_{13}	18.2445	0.0107	52	P ?
f_1	21.1416	0.0775	194	P
f_2	20.7177	0.0432	137	P
f_{102}	20.6659	0.0026	12	
f_{143}	20.2979	0.0017	8	?
f_{146}	20.9866	0.0016	8	
f_{153}	20.6632	0.0014	7	$f_2 - 5f_{orb}$
f_{164}	20.7191	0.0011	5	
f_{172}	20.6685	0.0010	5	$f_2 - 4f_{orb}$
f_{12}	21.9842	0.0114	50	P
f_{37}	21.9815	0.0049	23	
f_{39}	21.9868	0.0046	22	
f_{160}	21.9895	0.0012	6	?
f_{174}	21.9789	0.0009	4	
f_{16}	22.3150	0.0096	45	P
f_{141}	22.3421	0.0018	9	?
f_8	23.1563	0.0184	81	P
f_{53}	23.2435	0.0039	20	$f_9 + f_2$; MC
f_{106}	23.3033	0.0025	13	
f_{110}	23.1577	0.0025	12	?
f_{140}	23.2760	0.0018	9	
f_{161}	23.1549	0.0012	6	
f_{170}	23.1603	0.0010	5	
f_{173}	23.1697	0.0010	5	
f_{178}	23.2786	0.0007	4	$12f_{orb} + f_8$

Notes. **P**: parent frequency. **MC**: Mode Coupling of a very dominant g mode and p mode . **(?)**: mathematically agrees to a very high multiple of f_{orb}. f_{orb} = 0.010 ± 0.02 d^{-1}.

5.2. The Kepler SC light curve

From the *Kepler* SC Fourier spectrum (see panel (b) of Fig. 4), we confirm the detection of seven p modes in common with the results from the *Kepler* LC spectrum. We imply to the detected significant frequencies from *Kepler* SC by fs. The most domi-

Table 8. Detected regularly-split p modes .

f_i	f (d^{-1})	A (mmag)	S/N	Δf
f_1	21.1416	0.0775	194	
f_{12}	21.9842	0.0114	50	0.8426
f_{16}	22.3150	0.0096	45	
f_8	23.1563	0.0184	81	0.8414
f_{160}	21.9895	0.0012	6	
f_{39}	21.9868	0.0046	22	0.0027
f_{12}	21.9842	0.0114	50	0.0027
f_{37}	21.9815	0.0049	23	0.0027
f_{174}	21.9789	0.0009	4	0.0026
f_{178}	23.2786	0.0007	4	
f_{140}	23.2760	0.0018	9	0.0027
f_{170}	23.1603	0.0010	5	
f_{110}	23.1577	0.0025	12	0.0026

Table 9. Well-resolved significant high-frequencies ($fs \geq 17.5$ d^{-1}) derived from the *Kepler* SC spectrum, sorted according to descending amplitude.

fs_i	f (d^{-1})	A (mmag)	S/N	comb.
fs_1	21.1415	0.1067	29	P
fs_2	20.7177	0.0556	23	
fs_3	18.9788	0.0448	28	P
fs_4	23.1567	0.0266	22	P
fs_{10}	22.3158	0.0136	15	P
fs_{11}	18.2435	0.0129	14	
fs_{20}	23.2444	0.0057	8	$fs_5 + fs_{10}$; MC
fs_{25}	23.3037	0.0032	5	$2fs_1 - fs_3$
fs_6	26.9547	0.0222	18	P
fs_{21}	28.2747	0.0052	6	
fs_{22}	25.7788	0.0047	6	
fs_{23}	26.5955	0.0036	4	
fs_{24}	25.6598	0.0032	4	$2fs_{10} - fs_3$
fs_{26}	391.4914	0.0029	4	(!)

Notes. fs_i: remarks the significant high-frequencies from SC *Kepler* light curve. 'P': parent frequency. 'MC': Mode Coupling. (*): a combination of two p modes .

nant p mode , fs_1 = 21.1415 d^{-1}, has an amplitude 27.5% larger than f_1 (As$_1$ = 0.107 mmag ,and S/N = 29). We detected nine independent p modes (S/N>6) between 18.2-23.41 d^{-1}. The larger $f_{\rm Nyq}$ of the SC spectrum (compared to the LC one) allowed us to detect five more frequencies in the range 25.6-28.3 d^{-1}, four of which are independent p modes (S/N>6). We detected combination frequencies with fs_1, fs_3 and fs_{10} (see Table 9). Next, a very high frequency fs_{26} = 391.49 d^{-1}was also detected with S/N slightly larger than 4.0 that is far away from $f_{\rm Nyq}$ of the *Kepler* SC data 734.1 d^{-1}and S/N = 4.42 (marked by (!) in Table 10 and Table 9). We present a close view of this frequency region in Fig. 7. Such very fast pulsations (~3.68 min) remind us of roAp-like pulsations (Kurtz 1978, 1982). However, since S/N is barely larger than 4, it does not - by itself - demonstrate the occurrence of pulsations of roAp-type.

Table 10. Well-resolved significant high-frequencies ($\nu > 0.3$ d^{-1}) derived from TESS spectra and sorted according to descending amplitude.

Obs.	ν_i	f (d^{-1})	A (mmag)	S/N	comb.
s14-15	ν_1	21.1402	0.0701	8	
30-min	ν_4	20.7152	0.0521	6	
	ν_7	18.9845	0.0323	4	
s14-15	ν_2	21.1411	0.0928	11	
2-min	ν_5	20.7182	0.0464	6	
	ν_6	23.1571	0.0375	5	
s40-41	ν_1	21.1416	0.1003	13	
2-min	ν_4	20.7187	0.0465	6	
	ν_5	18.9808	0.0449	7	
	ν_6	23.1577	0.0353	5	
s40-41	ν_4	21.1418	0.1031	13	
2-min	ν_7	20.7180	0.0510	7	
CBV	ν_8	18.9804	0.0433	6	
corrected	ν_{10}	23.1575	0.0381	5	
	ν_{11}	26.9565	0.0275	4	
s54-55	ν_3	21.1700	0.0412	4	
2-min	ν_5	21.0714	0.0361	4	
	ν_6	20.9913	0.0352	4	
s54-55	ν_2	21.1411	0.0928	11	
2-min	ν_5	18.9776	0.0485	6	
CBV	ν_6	20.7182	0.0464	6	
corrected	ν_7	23.1571	0.0375	5	
	ν_8	318.9239	0.0286	4	(!)

Notes. ν_i: remarks the amplitude-sorted frequencies from different TESS light curves. 'P': parent frequency. The error on the frequencies and the amplitudes are of the order of 10^{-3} d^{-1}and 10^{-3} mmag, respectively.

5.3. The TESS light curves

Table 10 reports the high frequencies $\nu \leq 17.5$ d^{-1}detected from the TESS light curves of different sectors and pipelines. We designate these frequencies with ν. We detected four p modes from TESS data in common with the *Kepler* results that are 21.14 d^{-1}, 20.71 d^{-1}, 18.98 d^{-1}, and 23.157 d^{-1}(e.g. f_2, f_4, and f_{110} in the *Kepler* LC spectra) and two p modes that are 26.95 d^{-1}and 20.99 d^{-1}(fs_6 and f_{146} in the *Kepler* SC spectra). The TESS light curves with a 2-min cadence have $f_{\rm Nyq}$ = 360.0 d^{-1}. A very high frequency ν_8 = 318.9239 d^{-1} (A = 0.0286 mmag, marked as (!) in Table 10) is also detected from the TESS customised CBV-corrected light curves of sectors 54-55. Similar to the very high frequency from Sect. 5.2, ν_8 has a S/N close to the detection limit (4.02). We couldn't detect this frequency in the original data of sectors 54-55 (without the CBV correction) nor from the other 2-min cadence sectors (Fig. 7). The value, furthermore, differs from the frequency detected in the *Kepler* SC light curve (~391

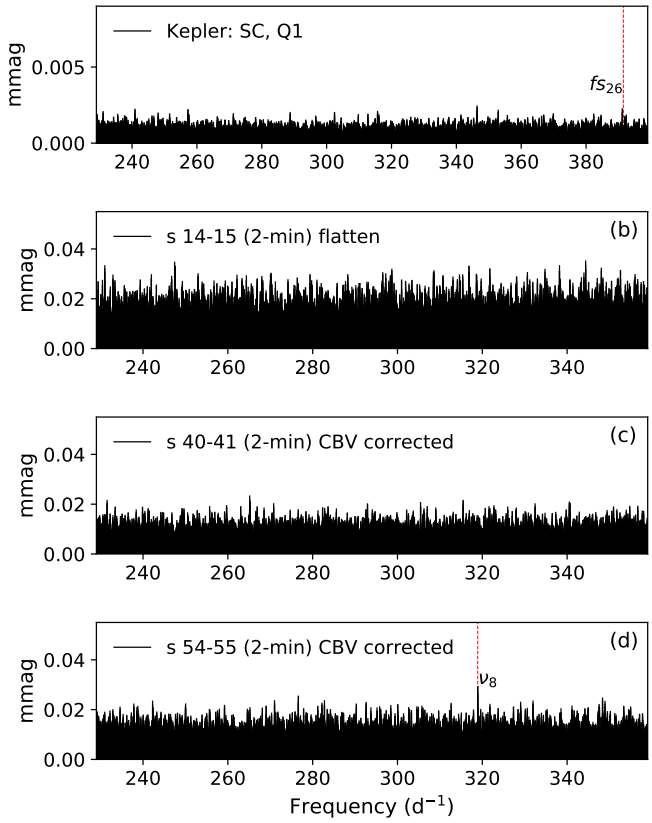

Fig. 7. A close view to the very high-frequency region of *Kepler* SC and TESS 2-min Fourier spectra (in black) where the false-positive (potential) roAp-like modes (in red) happen.

d^{-1}). The target is observed by camera 3 in sectors 54-55 that are not experiencing any light scatter due to Earth/Moon. More over, the contamination effect on TESS observations (see Table 3)is twice *Kepler* but ignorable. Hence we don't expect these larger frequencies appear as a result of any type of contamination.

6. Detection of γ Dor-type pulsations

6.1. The Kepler LC light curve

Fig. 8 panel (a) illustrates a close view of the low-frequency region of the *Kepler* LC Fourier spectrum. The parent g modes are grouped in four intervals 0.71-0.79, 0.85-0.89, 2.49-2.54 d^{-1} and 2.94-3.00 d^{-1}, three of which are presented in panels (b), (c), and (d) of Fig. 8. Table 11 reports the characteristics of each frequency group in order of descending amplitude. Next, we describe the major features of each group.

- **0.71-0.79 d^{-1}**: f_{78} = 0.71 d^{-1} is the most significant frequency in this group. It shows splitting by f_{orb} (i.e. f_{112}).
- **0.85-0.89 d^{-1}**: The most dominant frequency f_3 = 0.8914 d^{-1} is located in this group. Balona (2013) assimilated f_3 with the rotation frequency $f_{\rm rot}$. f_3 is coupled with $f_{\rm orb}$ to form f_{116} = 0.8814 d^{-1}. Better to mention that we also recognised f_{33} as a (potential) large harmonic of $f_{\rm orb}$ (indicated by (?) in Table 11). We couldn't find any regular period spacing pattern for the frequencies of this group.

Table 11. Well-resolved frequencies in low-frequency region of the *Kepler* LC spectrum.

$f_{\rm i}$	f (d^{-1})	A (mmag)	S/N	comb.
f_{78}	0.7100	0.0031	5	
f_{95}	0.7134	0.0027	4	
f_{112}	0.7198	0.0024	4	f_{78} + $f_{\rm orb}$
f_{132}	0.7887	0.0021	4	
f_3	0.8914	0.0354	46	P; $f_{\rm rot}$
f_{17}	0.8788	0.0093	13	P
f_{21}	0.8775	0.0083	12	
f_{33}	0.8754	0.0053	7	?
f_{116}	0.8814	0.0024	4	$f_3 - f_{\rm orb}$
f_{11}	2.4196	0.0126	30	P
f_9	2.5258	0.0135	32	P
f_{14}	2.5228	0.0106	26	P
f_{72}	2.5207	0.0033	8	$2f_{14} - f_9$
f_{100}	2.5280	0.0026	7	$2f_9 - f_{14}$; ?
f_{142}	2.5336	0.0018	4	$2f_{12} - 2f_2$ (*)
f_{77}	2.5668	0.0032	8	?
f_{145}	2.5181	0.0017	4	?
f_{150}	2.5001	0.0015	4	
f_{117}	2.4976	0.0024	6	?
f_{20}	2.8431	0.0084	23	P
f_{93}	2.9445	0.0027	8	
f_{119}	2.9703	0.0023	7	

Notes. (*): a combination of two p modes . **P**: parent frequency. **(?)**: mathematically agrees to a very high multiple of $f_{\rm orb}$.

- **2.49-2.54 d^{-1}**: f_9 = 2.5258 d^{-1}, the second highest amplitude g mode is located in this region. We identified f_{72} = 2.5207 d^{-1} as a combination of f_9 and f_{14} while f_{142} is a combination of f_2 and a p mode (f_{12} in Table 7). We detected three potentially large harmonics of $f_{\rm orb}$ (Table 11). We did not detect any regular period spacing among five neighbours of f_9.
- **2.94-3.00 d^{-1}**:
  The frequencies in this group are independent.

We also detected an independent single dominant g mode , f_{11} = 2.4196 d^{-1}. f_{20}=2.8431 d^{-1}is another stand-alone g mode detected not linked to the nearby parent g modes f_{93} and f_{119}.
Two doublets with a common spacing of 0.0027 d^{-1}were detected (Table 13), showing the same spacing as the one found in some p modes (Sect. 5). We also studied the amplitude evolution of the detected g modes across the orbital cycle (see Figure A2). We detected several significant frequencies approximately grouped in the vicinity of the frequencies f_6 = 5.0483 d^{-1}, f_5 = 5.7332 d^{-1}, and f_{25}=7.5725 d^{-1}(see panel (a) of Fig.8). The most dominant frequencies centred at f_5 = 5.7332 d^{-1}have a mean S/N of 49±20, and a mean amplitude of 0.016±0.007 mmag. Barceló Forteza et al. (2020) derived a minimum rotation rate of 70% for KIC 7756853. We noticed that the groups around f_6 and f_5 have frequencies slightly smaller than 6-7 times $f_{\rm rot}$, suggestive of (probable) r modes (see Fig. 8 where we divided the Fourier spectra with magenta solid lines into regions in-between the $f_{\rm rot}$ harmonics). From all 22 detected frequencies located in the in-

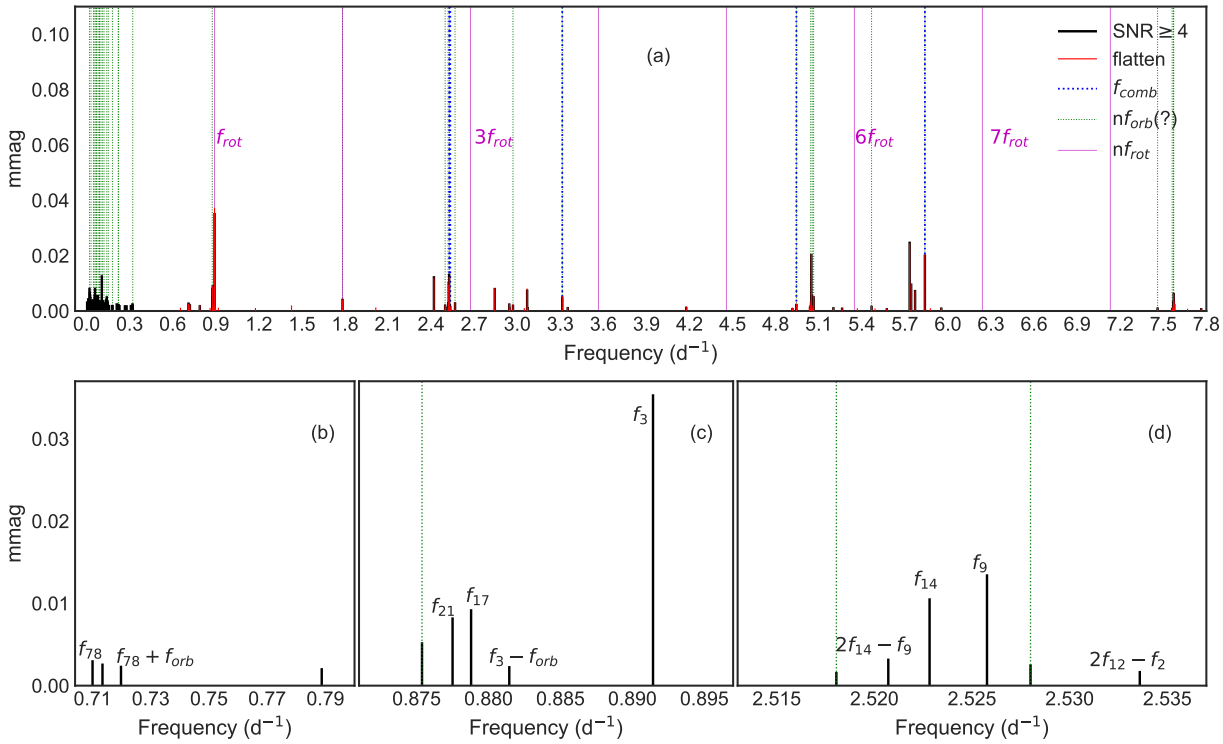

Fig. 8. A portion of the low-frequency region of the *Kepler* LC spectrum. The frequencies shown in black are the well-resolved significant frequencies.

terval 4.9-8.0 d^{-1}, only seven were identified as combinations of the parent frequencies f_9, f_{11}, f_{14}, and f_{93}.

6.2. The Kepler SC light curve

We report the detection of three low-frequency modes from *Kepler* SC spectrum in common with the results of the *Kepler* LC spectrum in Table 14. These frequencies are fs_5 = 0.8926 d^{-1}($f_{\rm rot}$), fs_{12} = 2.4186 d^{-1}($\sim f_{11}$), and fs_{17} = 2.8460 d^{-1}($\sim f_{20}$) and they are illustrated in panel (b) of Fig. 4. As in Sect. 6.1, we detected a couple of frequencies in-between 5.0-7.0 d^{-1}, two of which are a combination of the parent p modes , fs_6 and fs_4, and fs_1.

6.3. The TESS light curves

We report the significant low frequencies detected from the TESS data in Table 15. This region is illustrated in (panels b, d, f, and h) of Fig. 5. The detection of low frequency modes is only successful with sectors 14-15 (30 min TESS-SPOC) and sectors 40-41 (2 min CBV-corrected). They show frequencies in the range 0.92-1.06 d^{-1}that are split by a mean spacing δf equal to 0.70±0.0019 d^{-1}. The other low-frequency mode ν_6 = 0.8653d^{-1}is a coupling of the p modes ν_1 = 21.1402 d^{-1}and ν_4 = 20.7152 d^{-1}. In the Fourier spectrum of sectors 40-41, we only detected ν_9 = 0.885 d^{-1}. Unlike the *Kepler* light curves, no significant frequency with $\nu \geq 5$ d^{-1}was detected in the TESS light curves.

7. Discussion & Conclusion

KIC 7756853 is a double-lined spectroscopic binary (SB2 of mean spectral type A3Vs) with an orbital period of 99.316 ± 0.020 d. It consists of two A-type stars for which the best set of atmospheric parameters gives $T_{\rm eff}$ = 9700 ± 300 K, $\log g$ = 4.7 ± 0.3 (component A), and $T_{\rm eff}$ = 7600 ± 300 K, $\log g$ = 4.0 ± 0.3 (component B). In our view, the resulting values of $T_{\rm eff}$ point to component B as the probable δ Sct – γ Dor hybrid pulsator, whereas component A lies outside the δ Scuti instability strip. However, the temperature difference seems to contradict the mass ratio obtained from the orbital parameters, namely q = 0.91 ± 0.06. Indeed, using the mass-luminosity relation for normal main-sequence stars (a = 3.9, e.g. Harwit 1998) and the spectroscopic mass ratio $q = 10^{-\Delta {\rm v}/(2.5K)}$, we find Δv = 0.4 mag and the associated luminosity fraction $B = 10^{-\Delta {\rm v}/2.5}$ = 0.69. On the main sequence, such a luminosity ratio would correspond to a smaller temperature difference (both stars would be similar). Although both components could in principle be true slow rotators, this is not expected from their effective temperatures well above 7000 K. From the values of the minimum masses, we can deduce that these are severely underestimated, which indicates that the orbital inclination must be small. Accordingly, the projected rotational velocities must also be underestimated. Hence, both companion stars are probably fast rotators, as expected for non-peculiar, early to mid-A-type stars (e.g. the discussion on v_{eq} in Royer et al. 2007).

Using the orbital parameters derived by Lampens et al. (2018), Murphy et al. (2018) found no evidence of the 99-d binary in the time delays of the pulsation frequencies to very high precision. These authors suggested that the binary would be part of a triple system with an outer component that could be the source of the

Table 12. Well-resolved frequencies in frequency region 5-10 $d^{-1}$of the *Kepler* LC spectrum.

f_i	f (d^{-1})	A (mmag)	S/N	comb.
f_6	5.0483	0.0206	65	$f_9 + f_{14}$
f_{29}	5.0504	0.0058	20	
f_{31}	5.0643	0.0054	18	?
f_{71}	5.0464	0.0033	12	
f_{98}	4.9443	0.0026	9	$f_{11} + f_9$
f_{133}	5.0440	0.0021	7	
f_{138}	5.0527	0.0020	7	
f_{144}	5.0396	0.0017	6	
f_{156}	5.0546	0.0014	5	
f_{139}	5.4680	0.0019	7	$f_{14} + f_{93}$
f_5	5.7332	0.0251	73	
f_7	5.8394	0.0204	64	$f_9 + f_{14}$
f_{15}	5.7438	0.0099	33	
f_{23}	5.7711	0.0076	26	
f_{157}	7.4603	0.0013	5	
f_{25}	7.5725	0.0065	26	?
f_{61}	7.5709	0.0037	15	$f_9 + 2f_{14}$
f_{63}	7.5736	0.0037	15	$f_{14} + 2f_9$
f_{104}	7.5762	0.0026	11	
f_{149}	7.5689	0.0015	6	
f_{162}	7.5667	0.0012	5	
f_{163}	7.5619	0.0011	5	

Notes. The frequencies are sorted according to descending amplitude. **(?)**: mathematically agrees to a very high multiple of f_{orb}. f_{orb} = 0.010±d^{-1}.

Table 13. Detected regularly-split g modes .

f_i	f (d^{-1})	A (mmag)	S/N	Δf
f_{112}	0.7198	0.0024	4	
f_{78}	0.7100	0.0031	5	0.0098
f_3	0.8914	0.0354	46	
f_{116}	0.8814	0.0024	4	0.0100
f_{100}	2.5280	0.0026	7	
f_{145}	2.5181	0.0017	4	0.0099
f_{116}	0.8814	0.0024	4	
f_{17}	0.8788	0.0093	13	0.0027
f_{72}	2.5207	0.0033	8	
f_{145}	2.5181	0.0017	4	0.0027

pulsations. On the other hand, a low orbital inclination for the binary system will reduce the resulting light-time effect.

We performed our frequency analysis for KIC 7756853 on *Kepler* LC light curve (Q0-Q17) and compared the results for all other available *Kepler* SC (Q1) and TESS (sectors 14-15, 40-41, 54-55) light curves. From the TESS observations, we employed TASOC, TESS-SPOC pipeline light curves of sectors 14-15, and SPOC pipeline of sectors 40-41, 54-55 alongside our customised CBV corrected light curves. From Fourier analysis of *Kepler* LC

Table 14. Well-resolved significant low frequencies ($fs > 0.3$ d^{-1}) derived from the *Kepler* SC spectrum, sorted according to decreasing amplitude.

fs_i	f (d^{-1})	A (mmag)	S/N	comb.
fs_5	0.8926	0.0252	7	
fs_9	2.5302	0.0138	7	
fs_{12}	2.4186	0.0122	7	
fs_{17}	2.8460	0.0076	5	
fs_{14}	3.0705	0.0092	6	
fs_7	5.7381	0.0209	12	
fs_{13}	5.8396	0.0109	7	$fs_6 - fs_1$; (*)
fs_{16}	5.0411	0.0079	6	
fs_{19}	7.5640	0.0069	5	$2fs_6 - 2fs_4$; (*)

Notes. The frequencies are sorted according to descending amplitude. fs_i: remarks the significant frequencies from SC *Kepler* light curve. 'P': parent frequency. 'MC': Mode Coupling. (*): a combination of two p modes .

Table 15. Well-resolved significant low frequencies ($\nu > 0.3$ d^{-1}) derived from TESS spectra.

Obs.	ν_i	f (d^{-1})	A (mmag)	S/N	comb.
s14-15	ν_2	0.9970	0.0659	5	
30-min	ν_3	0.9288	0.0575	5	
	ν_5	1.0696	0.0491	4	
	ν_6	0.8653	0.0488	4	$2\nu_1 - 2\nu_4$
s40-41 2-min CBV corrected	ν_9	0.8858	0.0386	4	

Notes. The frequencies are sorted according to descending amplitude (see Sect. 6.3). ν_i: remarks the amplitude-sorted frequencies from different TESS light curves. 'P': parent frequency. The error on the frequencies and the amplitudes are of the order of 10^{-3} $d^{-1}$and 10^{-3} mmag, respectively.

light curve, we detected in total 179 significant frequencies, 20 of which are $f \leq 25.0$ (S/N$\geq$ 5) δ Scuti-type pulsations and 7 of which are detected in common with all other observations but with slightly larger amplitudes in some cases. We associate the non-detection of some p modes from SC and TESS spectra to their large f_{res} compared to the LC spectrum. We report the detection of an extra 3 p modes $f \geq 25$ d^{-1}(S/N $\geq$ 6) from the SC spectrum, one of which is also detected from TESS sectors 40-41 (2-min) observations. We detected three p modes to be equally split by harmonics of f_{orb}. We can't relate the other detected equally-split frequencies, Δf =0.0027 d^{-1}($\approx$ a 1-year period) and Δf = 0.84 $d^{-1}$to any origin with an astrophysical explanation.

From the frequency analysis of the *Kepler* LC spectrum in the frequency region 0.3-10.0 d^{-1}, we detected up to 13 g modes (S/N$\geq$ 5) in the range 2.49-2.53 $d^{-1}$and a candidate rotation frequency (Balona 2018) of f_3 = 0.8914 d^{-1}. We detected

a group of three low-frequencies at 0.71 d^{-1}one split by f_{orb} but with S/N of 4-5 σ. The frequencies grouped at 2.52 $d^{-1}$are slightly smaller than $3f_3$. Considering that the minimum rotation rate of the secondary star is 70% of its Keplerian value (i. e. an intermediate-to-fast rotator), these modes are (potentially) suggestive of r modes (Saio et al. 2018) with an azimuthal order m=3. A similar example is also detected in the KIC 8975515 LC spectrum by (Samadi-Ghadim et al. 2020). We detected three groups of significant frequencies with the most significant modes 5.084 d^{-1}, 5.7332 d^{-1}, and 7.5725 d^{-1}, seven of which are a combination of parent g modes . The first two groups are (5.084 d^{-1}, and 5.7332 d^{-1}) sandwiched between 6-7 harmonics of candidate rotation frequency. We couldn't recognise any regular period spacing pattern among the g modes .

We attribute the δ Scuti-type pulsations to the second component and we suggest most probably KIC 7756853B is a hybrid intermediate to fast rotator δ Sct – γ Dor stars with a potential of having r modes . this conclusion is based on following causes. First: The secondary star has a lower temperature (corresponding to an A5-type star with T_{eff} = 7600 ± 300 K) that locates it in the middle of the δ Scuti Instability Strip. By suggesting a maximum orbital inclination of $i_{orb} \sim 27$ deg and information in Table 2, while we assume f_3 as f_{rot_B} we estimate a $R_B = 2.49 \pm 0.15\ R_\odot$ limit for the secondary radius and a mass of $M_B \sim 1.71\ M_\odot$(and relatively $M_A = 1.87 \pm 0.02\ M_\odot$ for the primary hotter companion). The estimation parameters agrees with the expected values (e.g. from table 5 Capitanio et al. 2017) for an A5-type star (in contrary to the assumption of $i_{orb} = 43$ deg from Barceló Forteza et al. (2020)). Hence, we infer f_3 as f_{rot} of the secondary star. Second, we detected three of the g modes to split by harmonics of f_{orb} including f_{rot}. We identified couple of modes to be a coupling of parent p modes , g modes , and the rotational frequency. We suggest the coupled modes, and the detected rotational frequency have the same origin, the secondary companion in KIC 7756853; and the last, the scatter in radial velocity (from the spectroscopic study) is significantly higher than for the primary although both stars present a small $v \sin i$.

Though, we detected frequency splittings as large as orbital frequency among three couple of g modes , but We do not expect tidal forces to influence the pulsation modes in KIC 7756853. This is because, with a maximum limit of 27 deg for the orbital inclination, we derive a semi-major axis of a ∼ 0.64 AU (a periastron distance of ∼0.43 AU *equiv* 91 $R_\odot$)that is large for the tidal forces to act upon pulsations through periastron passage. We can not relate the detected equally-split frequencies, Δf =0.0027 d^{-1}(≈ 1 year) to any nature with the astrophysical explanation.

From the evolution of the g modes over the available orbital cycles, we detected a considerable amplitude modulation (σ_A = 0.007 mmag) for the rotation frequency in comparison to other g modes ($\sigma_A \sim 0.0015$ mmag). This is also the case for f_{11} = 2.5258 $d^{-1}$with a $\sigma_A \sim 0.006$ mmag suggestive of a potential chemical spot, which we can not confirm due to lack of chemical abundances studies.

We detected two very different roAp-like high frequencies from the SC light curve and our customised CBV corrected TESS 54-55 sectors. The fact that the two detected independent frequencies are very different and their S/N is very close to the 4, prevents us from confirming the origin of these frequencies ass roAp pulsations. Similarly, due to the insufficient S/N of the HERMES composite spectra for KIC 7756853, it is not possible to search for Ap-like Chemical abundances. Hence, we delay it to the time when we have better S/N spectroscopic and photometric observations.

Acknowledgements. This paper includes data collected by the Kepler mission and obtained from the MAST data archive at the Space Telescope Science Institute (STScI). Funding for the Kepler mission is provided by the NASA Science Mission Directorate. STScI is operated by the Association of Universities for Research in Astronomy, Inc., under NASA contract NAS 5–26555. This paper also includes data collected by the TESS mission. Funding for the TESS mission is provided by the NASA's Science Mission Directorate.

References

Aerts, C., Christensen-Dalsgaard, J., & Kurtz, D. W. 2010, Asteroseismology
Antoci, V., Cunha, M., Houdek, G., et al. 2014, ApJ, 796, 118
Antoci, V., Cunha, M. S., Bowman, D. M., et al. 2019, MNRAS, 490, 4040
Bailer-Jones, C. A. L., Rybizki, J., Fouesneau, M., Demleitner, M., & Andrae, R. 2021, AJ, 161, 147
Balmforth, N. J., Cunha, M. S., Dolez, N., Gough, D. O., & Vauclair, S. 2001, MNRAS, 323, 362
Balona, L. A. 2013, MNRAS, 431, 2240
Balona, L. A. 2018, MNRAS, 476, 4840
Balona, L. A., Daszyńska-Daszkiewicz, J., & Pamyatnykh, A. A. 2015, MNRAS, 452, 3073
Balona, L. A. & Dziembowski, W. A. 2011, MNRAS, 417, 591
Barceló Forteza, S., Moya, A., Barrado, D., et al. 2020, A&A, 638, A59
Breger, M. 2000, in Astronomical Society of the Pacific Conference Series, Vol. 210, Delta Scuti and Related Stars, ed. M. Breger & M. Montgomery, 3
Breger, M., Stich, J., Garrido, R., et al. 1993, A&A, 271, 482
Brown, T. M., Latham, D. W., Everett, M. E., & Esquerdo, G. A. 2011, AJ, 142, 112
Caldwell, D. A., Tenenbaum, P., Twicken, J. D., et al. 2020, Research Notes of the American Astronomical Society, 4, 201
Capitanio, L., Lallement, R., Vergely, J. L., Elyajouri, M., & Monreal-Ibero, A. 2017, A&A, 606, A65
Christensen-Dalsgaard, J. 2000, in Astronomical Society of the Pacific Conference Series, Vol. 210, Delta Scuti and Related Stars, ed. M. Breger & M. Montgomery, 187
Cox, A. N. 2000, Allen's astrophysical quantities
Cunha, M. S., Alentiev, D., Brandão, I. M., & Perraut, K. 2013, MNRAS, 436, 1639
D'Antona, F., Caloi, V., Montalbán, J., Ventura, P., & Gratton, R. 2002, A&A, 395, 69
Duchêne, G. & Kraus, A. 2013, ARA&A, 51, 269
Dupret, M. A., Grigahcène, A., Garrido, R., et al. 2005, MNRAS, 360, 1143
Dupret, M.-A., Grigahcène, A., Garrido, R., Gabriel, M., & Scuflaire, R. 2004, A&A, 414, L17
Grigahcéne, A., Antoci, V., Balona, L., et al. 2010, ApJ, 713, L192
Guo, Z., Fuller, J., Shporer, A., et al. 2019, ApJ, 885, 46
Guo, Z., Gies, D. R., & Matson, R. A. 2017, ApJ, 851, 39
Guzik, J. A., Kaye, A. B., Bradley, P. A., Cox, A. N., & Neuforge, C. 2000, ApJ, 542, L57
Halbwachs, J.-L., Pourbaix, D., Arenou, F., et al. 2022, arXiv e-prints, arXiv:2206.05726
Hambleton, K. M., Kurtz, D. W., Prša, A., et al. 2013, MNRAS, 434, 925
Handler, G. 1999, MNRAS, 309, L19
Handler, G. 2013, Asteroseismology, ed. T. D. Oswalt & M. A. Barstow, Vol. 4, 207
Harwit, M. 1998, Astrophysical concepts
Holdsworth, D. L., Cunha, M. S., Kurtz, D. W., et al. 2021, MNRAS, 506, 1073
Houdek, G., Balmforth, N. J., Christensen-Dalsgaard, J., & Gough, D. O. 1999, A&A, 351, 582
Huang, C. X., Vanderburg, A., Pál, A., et al. 2020a, Research Notes of the American Astronomical Society, 4, 204
Huang, C. X., Vanderburg, A., Pál, A., et al. 2020b, Research Notes of the American Astronomical Society, 4, 206
Jenkins, J. M. 2017, Kepler Data Processing Handbook: Overview of the Science Operations Center, Kepler Science Document KSCI-19081-002, id. 2, Edited by Jon M. Jenkins.
Jenkins, J. M., Twicken, J. D., McCauliff, S., et al. 2016, in Society of Photo-Optical Instrumentation Engineers (SPIE) Conference Series, Vol. 9913, Software and Cyberinfrastructure for Astronomy IV, ed. G. Chiozzi & J. C. Guzman, 99133E
Kaye, A. B., Handler, G., Krisciunas, K., Poretti, E., & Zerbi, F. M. 1999, PASP, 111, 840
Keen, M. A., Bedding, T. R., Murphy, S. J., et al. 2015, MNRAS, 454, 1792
Koch, D. G., Borucki, W. J., Basri, G., & et al. 2010, ApJ, 713, L79
Kunimoto, M., Huang, C., Tey, E., et al. 2021, Research Notes of the American Astronomical Society, 5, 234
Kurtz, D. W. 1978, Information Bulletin on Variable Stars, 1436, 1

Kurtz, D. W. 1982, MNRAS, 200, 807
Lampens, P. 2021, Galaxies, 9, 28
Lampens, P., Frémat, Y., Vermeylen, L., et al. 2018, A&A, 610, A17
Lee, J. W. 2016, ApJ, 833, 170
Lightkurve Collaboration, Cardoso, J. V. d. M., Hedges, C., et al. 2018, Lightkurve: Kepler and TESS time series analysis in Python, Astrophysics Source Code Library
Lomb, N. R. 1976, Ap&SS, 39, 447
Lund, M. N., Handberg, R., Buzasi, D. L., et al. 2021, ApJS, 257, 53
Lund, M. N., Handberg, R., Davies, G. R., Chaplin, W. J., & Jones, C. D. 2015, ApJ, 806, 30
Lund, M. N., Handberg, R., Kjeldsen, H., Chaplin, W. J., & Christensen-Dalsgaard, J. 2017, in European Physical Journal Web of Conferences, Vol. 160, European Physical Journal Web of Conferences, 01005
Ma, S., Esamdin, A., Hernández, A. G., et al. 2022, ApJ, 937, 80
Moe, M. & Di Stefano, R. 2017, ApJS, 230, 15
Murphy, S. J., Moe, M., Kurtz, D. W., et al. 2018, MNRAS, 474, 4322
Murphy, S. J., Saio, H., Takada-Hidai, M., et al. 2020, MNRAS, 498, 4272
Niemczura, E., Murphy, S. J., Smalley, B., et al. 2015, MNRAS, 450, 2764
Ricker, G. R., Winn, J. N., Vanderspek, R., et al. 2014, in Society of Photo-Optical Instrumentation Engineers (SPIE) Conference Series, Vol. 9143, Space Telescopes and Instrumentation 2014: Optical, Infrared, and Millimeter Wave, ed. J. Oschmann, Jacobus M., M. Clampin, G. G. Fazio, & H. A. MacEwen, 914320
Ricker, G. R., Winn, J. N., Vanderspek, R., et al. 2015, Journal of Astronomical Telescopes, Instruments, and Systems, 1, 014003
Royer, F., Zorec, J., & Gómez, A. E. 2007, A&A, 463, 671
Saio, H. 2005, MNRAS, 360, 1022
Saio, H., Kurtz, D. W., Murphy, S. J., Antoci, V. L., & Lee, U. 2018, MNRAS, 474, 2774
Samadi, A., Jassur, D. M. Z., Nassiri, S., et al. 2010, New A, 15, 339
Samadi-Ghadim, A., Lampens, P., & Gizon, L. 2022, A&A, 667, A60
Samadi-Ghadim, A., Lampens, P., & Jassur, D. 2018a, Acta Astron., 68, 425
Samadi-Ghadim, A., Lampens, P., & Jassur, D. 2018b, MNRAS, 474, 5549
Samadi-Ghadim, A., Lampens, P., Jassur, D. M., & Jofré, P. 2020, A&A, 638, A57
Scargle, J. D. 1982, ApJ, 263, 835
Schmid, V. S., Tkachenko, A., Aerts, C., et al. 2015, A&A, 584, A35
Sekaran, S., Tkachenko, A., Abdul-Masih, M., et al. 2020, A&A, 643, A162
Sekaran, S., Tkachenko, A., Johnston, C., & Aerts, C. 2021, A&A, 648, A91
Southworth, J. 2021, The Observatory, 141, 282
Stassun, K. G., Oelkers, R. J., Paegert, M., et al. 2019, AJ, 158, 138
Uytterhoeven, K., Moya, A., Grigahcène, A., et al. 2011, A&A, 534, A125
Van Reeth, T., Johnston, C., Southworth, J., et al. 2023, A&A, 671, A121
Xiong, D. R., Deng, L., Zhang, C., & Wang, K. 2016, MNRAS, 457, 3163
Zhang, X., Chen, X., Zhang, H., Fu, J., & Li, Y. 2020, ApJ, 895, 124

List of Objects

Table A1. Logbook and overview of the acquired HERMES spectra for KIC 7756853.

Date	Exp. [s]	BJD	$SNR_{6500Å}$
20100601	1600	2455349.6467847	78.69
20100819	1800	2455428.4925475	121.54
20140816	500	2456886.4429460	48.56
20141107	800	2456969.4061808	–
20141112	650	2456974.3533371	65.06
20150515	1500	2457158.7074914	76.36
20150521	550	2457164.6144537	62.83
20150804	500	2457239.6666996	51.03
20150806	700	2457241.5899110	62.69
20151003	1000	2457299.3759516	24.20
20151028	1000	2457324.3448617	66.74
20160501	1000	2457510.6619398	65.40
20160504	900	2457513.6579595	66.38
20160608	550	2457548.7087928	52.71
20170522	666	2457896.5249552	60.45
20170805	700	2457971.5539826	65.08
20170808	1200	2457974.5838777	63.81
20170815	500	2457981.6270879	53.70
20170823	500	2457989.5395247	46.98
20180316	500	2458194.7065775	60.13
20190710	360	2458675.5581784	57.26
20191017	550	2458774.3767793	71.06
20191103	460	2458791.3183567	67.37
20190914	1040	2458741.4096710	58
20190917	2100	2458744.3556940	66
20190919	900	2458746.2677990	61
20190920	800	2458747.4469020	61
20190922	1200	2458749.4505050	65
20200917	750	2459110.4654409	52.01
20210627	550	2459393.5516002	56.95
20211009	550	2459497.3999509	59.00

Table A2. The relevant time information for all LC bins.

bin	start BKJD	start phase	end BKJD	end phase	T d	f_{res} d^{-1}
1	120.538941	0.24	147.021986	-0.49	26.483	0.038
2	147.042420	-0.49	177.060336	-0.19	30.018	0.033
3	177.080770	-0.19	204.503136	0.09	27.422	0.036
4	204.523569	0.09	230.147285	0.35	25.624	0.039
5	230.167719	0.35	257.486920	-0.38	27.319	0.037
6	257.507353	-0.38	285.500394	-0.10	27.993	0.036
7	285.520827	-0.10	311.633820	0.17	26.113	0.038
8	311.654252	0.17	338.931927	0.44	27.278	0.037
9	338.952360	0.44	367.108962	-0.27	28.157	0.036
10	367.129395	-0.27	393.345324	-0.01	26.216	0.038
11	393.365757	-0.01	422.647312	0.29	29.282	0.034
12	422.667746	0.29	449.170826	-0.45	26.503	0.038
13	449.191260	-0.45	474.448155	-0.19	25.257	0.040
14	474.468589	-0.19	500.972100	0.07	26.504	0.038
15	500.992535	0.07	526.923803	0.34	25.931	0.039
16	526.944237	0.34	553.467795	-0.40	26.524	0.038
17	553.488229	-0.40	579.500577	-0.14	26.012	0.038
18	579.521011	-0.13	605.675906	0.13	26.155	0.038
19	605.696340	0.13	631.769051	0.39	26.073	0.038
20	631.789484	0.39	657.024084	-0.35	25.235	0.040
21	657.044516	-0.35	683.034924	-0.09	25.990	0.038
22	683.055356	-0.09	709.168371	0.17	26.113	0.038
23	709.188804	0.17	750.749551	-0.41	41.561	0.024
24	750.769985	-0.41	778.723014	-0.13	27.953	0.036
25	778.743447	-0.13	810.273052	0.19	31.530	0.032
26	810.293487	0.19	835.611587	0.44	25.318	0.039
27	835.632021	0.44	861.502045	-0.30	25.870	0.039
28	861.522480	-0.30	888.352922	-0.03	26.830	0.037
29	888.373357	-0.03	914.488345	0.24	26.115	0.038
30	914.508779	0.24	940.623474	-0.50	26.115	0.038
31	940.643908	-0.50	965.818216	-0.25	25.174	0.040
32	965.838650	-0.25	991.932007	0.02	26.093	0.038
33	991.952440	0.02	1018.474424	0.28	26.522	0.038
34	1018.494857	0.29	1044.832684	-0.45	26.338	0.038
35	1044.853116	-0.45	1073.479300	-0.16	28.626	0.035
36	1073.499733	-0.16	1099.980708	0.11	26.481	0.038
37	1100.001141	0.11	1129.138843	0.40	29.138	0.034
38	1129.159276	0.40	1155.273415	-0.34	26.114	0.038
39	1155.293848	-0.34	1185.842685	-0.03	30.549	0.033
40	1185.863119	-0.03	1211.283428	0.23	25.420	0.039
41	1211.303863	0.23	1237.562154	0.49	26.258	0.038
42	1237.582588	0.49	1263.779548	-0.25	26.197	0.038
43	1263.799982	-0.25	1297.741201	0.10	33.941	0.029
44	1297.761636	0.10	1324.121356	0.36	26.360	0.038
45	1324.141790	0.36	1350.214968	-0.37	26.073	0.038
46	1350.235401	-0.37	1377.615791	-0.10	27.380	0.037
47	1377.636224	-0.10	1402.932106	0.16	25.296	0.040
48	1402.952538	0.16	1434.827540	0.48	31.875	0.031
49	1434.847973	0.48	1460.899737	-0.26	26.052	0.038
50	1460.920170	-0.26	1498.496594	0.12	37.576	0.027
51	1498.517027	0.12	1523.936356	0.37	25.419	0.039
52	1523.956790	0.37	1550.439180	-0.36	26.482	0.038

Notes. 'phase' is referring to orbital phase. 'T' is the time span of the observations.

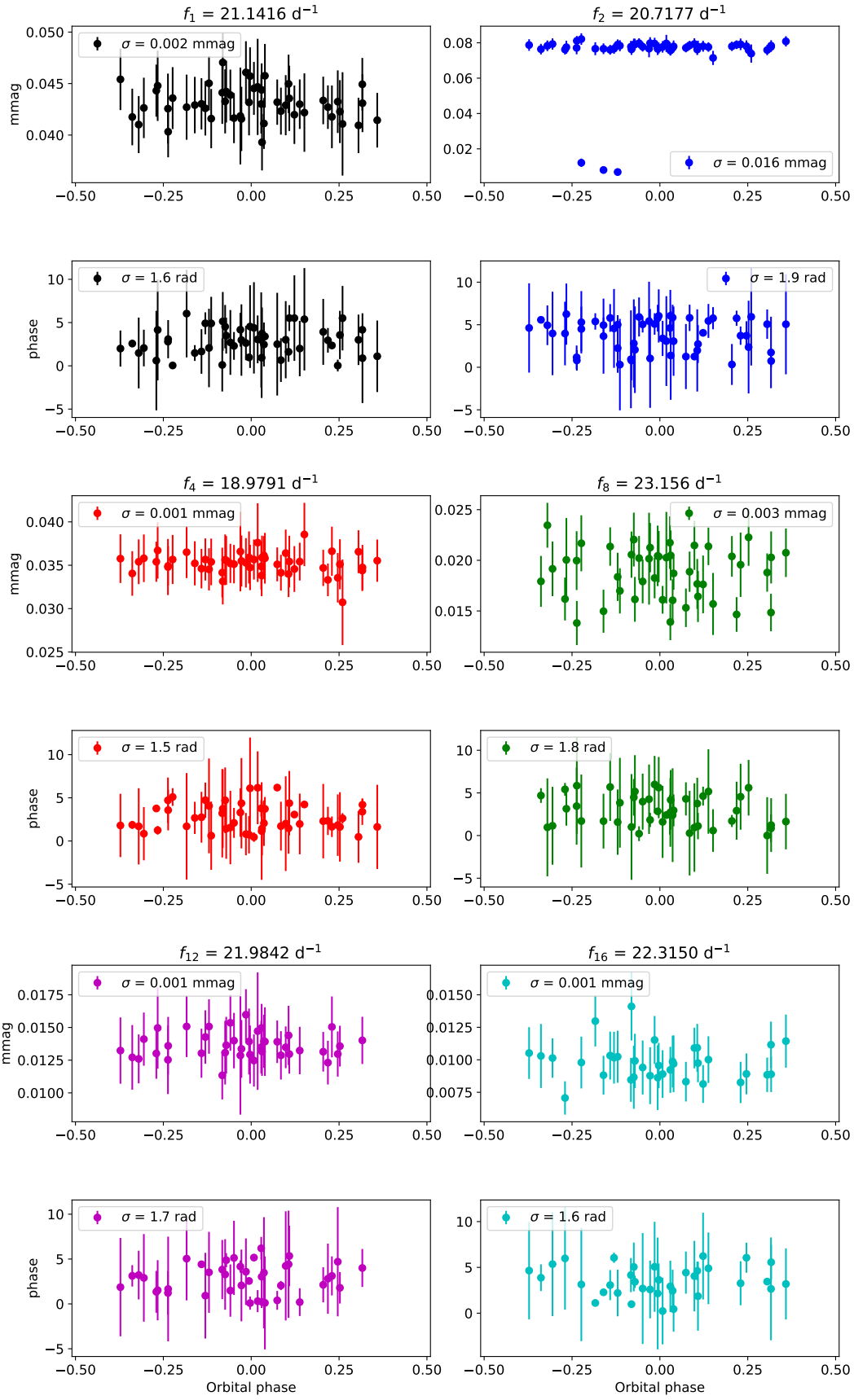

Fig. A1. Amplitude and phase variations across orbital phase for the most dominant p modes derived from the *Kepler* LC light curve.

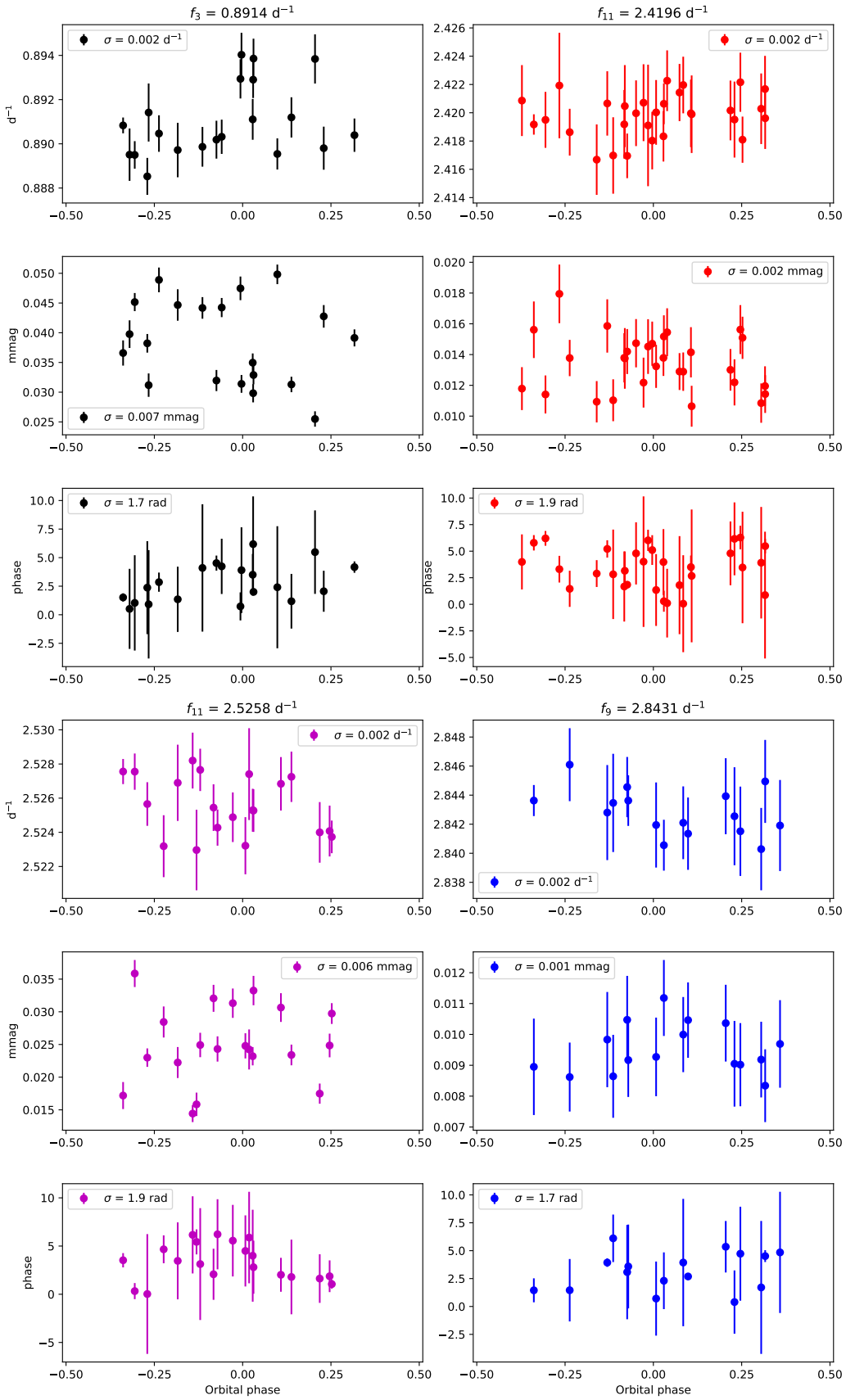

Fig. A2. Amplitude and phase variations in orbital cycle for the most dominant *g* modes derived from *Kepler* LC light curve.